Check for updates

ARTICLE   OPEN

Effects of iron corrosion products on the degradation of bentonite structure and properties

Yupeng Sun[1,2], Yangtao Zhou[2], Xin Wei[2 ✉], Junhua Dong [2 ✉], Nan Chen[2], Qiying Ren[2], Junhu Wang[3] and Wei Ke[4]

Bentonite is a key material for engineering barriers to prevent groundwater and nuclide migration in the multi-barrier system of high-level radioactive waste (HLW) geological disposal. However, its barrier property will be degraded under the action of iron corrosion products of steel disposal containers. In this paper, the effects of iron corrosion products on the degradation of bentonite structure and properties were investigated in the simulated environments for HLW geological disposal. The results showed that Fe^{2+}/Fe^{3+} dissolved from iron powder could enter montmorillonite (Mt) interlayer and substituted part of Na^+, which caused the decrease of the volume and interlayer spacing of Mt, and the structural integrity of Mt was destroyed. Macroscopically, the water absorption and swelling property of bentonite were significantly decreased. The degradation mechanism of Mt structure was mainly that Fe^{2+}/Fe^{3+} generated by iron corrosion entered the interlayer domain of Mt to compensate for the interlayer charge deficit.

INTRODUCTION

Deep geological disposal is generally accepted by most countries as the only feasible scheme to treat high-level radioactive waste (HLW), which mainly adopts the multi-barrier system to permanently isolate HLW from the living environment[1–3]. In the multi-barrier system, the iron-based container and buffer/backfill material are the key engineering materials to prevent nuclide leakage[4]. Among them, the corrosion resistance of iron-based container is the core element to meet the stability and durability of the repository system[5]. For the buffer/backfill material filled between the surrounding rock and the metal container, it should have appropriate mechanical properties and buffering capacity[6,7]. Its main function is to relieve the pressure of surrounding rock on metal containers. When the container fails due to corrosion perforation, it can also effectively block the migration of radionuclides to the surrounding environment[8]. Therefore, in the deep geological disposal of HLW, the buffer/backfill material system plays a crucial role in engineering barrier, hydraulic barrier and chemical barrier as well as the conduction and dissipation of heat from radioactive waste decay, and it is an effective guarantee for the long-term safety and stability of the geological repository of HLW[9,10]. However, it will face the threat of destabilization and degradation with the disposal, which can accelerate the leakage of nuclide, and then bring great harm to international public health and ecological environment.

Bentonite has been selected by many countries as the buffering material for the geological repository of HLW because of its extremely low water conductivity and good nuclide adsorption properties[11]. Montmorillonite (Mt) is the main mineral component that swells when bentonite absorbs water or solutions[12]. The crystal structure of Mt belongs to the monoclinic system, and each unit layer is composed of one Al-O octahedral sheet and two Si-O tetrahedral sheets. The surface of the Mt lamellar layer is negatively charged due to the isomorphic substitution of Mg^{2+}/Fe^{2+} for Al^{3+} in octahedral sheet and/or Al^{3+} for Si^{4+} in tetrahedral sheet, and the negative charge can be balanced by interlayer cations such as Na^+, K^+, Ca^{2+} or Mg^{2+}[12,13]. These interlayer cations are commonly hydrated and exchangeable, thus bentonite has a strong water swelling capacity, cation adsorption capacity and cation exchange capacity (CEC)[14,15]. Groundwater usually contains cations such as K^+, Ca^{2+} and Na^+, which have an important impact on the structure and buffering performance of Mt. Egloffstein reported that Ca^{2+} in the salt solution can easily substitute Na^+ of Mt interlayers in bentonite, thus decreasing the interlayer spacing and swelling capacity of Mt[16]. Karnland et al. found that Mt could be dissolved under high pH value (pHå 12) and generate non-swelling minerals[17–19]. Furthermore, the porosity and permeability of bentonite increased, while the buffering barrier performance decreased[20]. When the concentration of these cations in the solution is too high, the negative charge of bentonite colloidal particles decreases under the action of electric neutralization, and the mutual repulsion decreases, resulting in the aggregation and sedimentation of bentonite colloidal particles[21]. This effect simply corresponds to the decrease of the thickness of the electric double layer with the increase of ionic strength, and the influence of ionic strength on the structure and properties of Mt deserves further study. Meanwhile, the cation adsorption capacity of bentonite will also significantly decrease. Furthermore, the collapse of Mt interlayer may further hinder cation exchange.

In the long-term geological disposal process, the buffering performance of bentonite is not only related to the composition and concentration of cations in groundwater but also largely depends on the amount of iron corrosion products (Fe^{2+}/Fe^{3+}) generated by the corrosion of its internal iron-based container[22]. The physical/chemical properties and buffering performance of bentonite are inevitably affected by the corrosion products generated at the iron-based container/bentonite interface as the container corrodes[23,24]. Moreover, the proportion of iron corrosion products in bentonite at different distances from iron-based

containers is varied, which has different effects on the buffering performance of bentonite. Previous studies mainly focused on the reaction between clay minerals and iron, and found that the properties of reaction products were related to experimental conditions such as reaction temperature, initial properties of clay minerals and solid/liquid ratio[25]. Lantenois et al. studied Mts with various crystal chemical compositions and discovered that only dioctahedral Mt was destabilized in the presence of iron[26]. The presence of Na^+ ions in the Mt interlayers and the higher contents of structural Fe^{3+} in the octahedral sheets can promote the alteration of Mt. In addition, the higher pH value (pH>7) was more favorable for the occurrence of such alterations. Perronnet et al. proposed that the heterogeneity of interlayer structure, interlayer charge and surface energy of Mt may also affect the reaction rate[27]. However, it is still unclear how the characteristics, structure and swelling capacity of bentonite are affected by the corrosion products dissolved from iron-based containers. Moreover, there is also no unified conclusion about the occurrence oxidation state of Fe^{3+}/Fe^{2+} produced by iron corrosion in Mt structure, whether they are only adsorbed on the surface of Mt and enter the Mt interlayer[28-30], or further migrate into the octahedral site of Mt like natural Fe^{3+} in iron-rich Mt[26,31-33]. Thus, it is necessary to carry out this research based on the deep geological disposal scheme of HLW in China and the groundwater characteristics of pre-selected site.

The nuclear waste storage will start with aerobic condition due to the presence of atmosphere in the construction period of repository. With the closure of repository, it turned into an anoxic environment. In order to simulate the evolution process of HLW disposal environment, iron powder, bentonite and simulated Beishan groundwater were thoroughly mixed in different proportions to form experimental systems. With increasing time, the residual trace oxygen in the mixed sample was gradually consumed, and the experimental system turned to an anoxic condition. The main purpose of this work is to study the effects of iron corrosion products on the mineral composition, microstructure and buffering performance of surrounding bentonite. By combining with the parameters variations of Mt interlayer exchangeable cation content, mineral composition, interlayer spacing, occurrence state of iron in Mt, water absorption and swelling capacity, it reveals the degradation mechanism of Mt structure. The research results provide an important theoretical basis for the formulation of China's HLW geological disposal scheme.

RESULTS AND DISCUSSION

Iron corrosion products

Figure 1 shows the XRD patterns of the corrosion product after 1:1 bentonite/iron powder reacted at 15% and 30% water content (B1_I1_W15, B1_I1_W30) for 90 days. It can be seen that the iron corrosion products of B1_I1_W15 sample are mainly Fe_3O_4/γ-Fe_2O_3 and α-FeOOH. Furthermore, the diffraction peaks of metallic iron are also detected, indicating that there was still iron powder in the mixed sample after 90 days of reaction. In contrast, γ-FeOOH is also detected in the iron corrosion products of B1_I1_W30 sample, which illustrates that the water content during the reaction of bentonite/iron powder has a great influence on the chemical compositions of the corrosion products. Meanwhile, the diffraction peaks of minerals such as Mt[25,34,35] and quartz[36,37] are also detected, meaning that a small amount of bentonite minerals are still contained in the corrosion products.

Figure 2 shows the corrosion morphology and Raman spectra of corrosion products of B1_I1_W15 and B1_I1_W30 samples reacted for 90 days. As shown in Fig. 2, the above B1_I1 samples consists of two kinds of aggregates: black iron corrosion products and brown/reddish brown degraded bentonite. The Raman spectrum

of point A in Fig. 2b shows typical bands corresponding to Fe_3O_4 (308 cm^{-1}, 396 cm^{-1}, 548 cm^{-1}, 675 cm^{-1})[38-40]. In comparison, the Raman spectra of point B in Fig. 2b$_1$ shows typical bands of α-FeOOH (207 cm^{-1}, 298 cm^{-1}, 383 cm^{-1})[39,41], γ-FeOOH (218 cm^{-1}, 252 cm^{-1})[41,42], and Fe_3O_4 (470 cm^{-1}, 679 cm^{-1})[38,43].

The Raman results obtained for the corrosion products in Fig. 2 are basically consistent with the XRD results in Fig. 1. The only difference is that α-FeOOH is not found in Fig. 2b, this is because it only shows the spectrum of corrosion products corresponding to the green dots in Fig. 2a. In addition, it can be inferred that Fe_3O_4 is the main corrosion product generated in the reaction of bentonite/iron powder, and the γ-FeOOH also be produced with the increase of water content. Among them, the α-FeOOH and γ-FeOOH can be produced by electrochemical oxidation and/or chemical oxidation of ferrous corrosion products such as $Fe(OH)_2$, $Fe_2(OH)_2CO_3$, $Fe_6(OH)_{12}CO_3$ and $Fe_6(OH)_{12}SO_4$[44,45]. Furthermore, partial α/γ-FeOOH (in particular γ-FeOOH that is more reactive) may be reduced to Fe_3O_4 under anoxic conditions[46-49].

CEC of Mt interlayers in bentonite

Table 1 shows that the contents of Na^+ and Fe^{2+}/Fe^{3+} in Mt interlayer of original GMZ Na-bentonite are $43.7 \cdot 10^{-2}$ mol kg^{-1} and $0.2 \cdot 10^{-2}$ mol kg^{-1}, respectively. The trace iron originally existing in bentonite are mainly Fe^{3+}, which can be reduced to Fe^{2+} by reacting with metallic iron[50]. After 100:1 bentonite/iron powder reacted at 15% water content (B100_I1_W15) for 30 days, 60 days and 90 days, the Na^+ contents in Mt interlayer are $43.2 \cdot 10^{-2}$ mol kg^{-1}, $41.9 \cdot 10^{-2}$ mol kg^{-1} and $41.5 \cdot 10^{-2}$ mol kg^{-1}, respectively. Meanwhile, the Fe^{2+}/Fe^{3+} contents are $0.2 \cdot 10^{-2}$ mol kg^{-1}, $0.9 \cdot 10^{-2}$ mol kg^{-1} and $1.3 \cdot 10^{-2}$ mol kg^{-1}, respectively. As the water content increases to 30% (B100_I1_W30), the Na^+ contents in Mt interlayer decrease to $42.1 \cdot 10^{-2}$ mol kg^{-1}, $39.4 \cdot 10^{-2}$ mol kg^{-1} and $37.5 \cdot 10^{-2}$ mol kg^{-1}, while the Fe^{2+}/Fe^{3+} contents increase to $0.9 \cdot 10^{-2}$ mol kg^{-1}, $2.6 \cdot 10^{-2}$ mol kg^{-1} and $3.2 \cdot 10^{-2}$ mol kg^{-1} respectively. For 1:1 bentonite/iron powder, the Na^+ contents in Mt interlayer are $41.5 \cdot 10^{-2}$ mol kg^{-1}, $25.7 \cdot 10^{-2}$ mol kg^{-1} and $24.3 \cdot 10^{-2}$ mol kg^{-1} after 30 days, 60 days and 90 days of reaction at 15% water content (B1_I1_W15), and the Fe^{2+}/Fe^{3+} contents are $1.2 \cdot 10^{-2}$ mol kg^{-1}, $9.9 \cdot 10^{-2}$ mol kg^{-1} and $10.7 \cdot 10^{-2}$ mol kg^{-1}, respectively. When the water content increases to 30% (B1_I1_W30), the Na^+ contents in Mt interlayer decrease to $35.2 \cdot 10^{-2}$ mol kg^{-1}, $18.1 \cdot 10^{-2}$ mol kg^{-1} and $16.2 \cdot 10^{-2}$ mol kg^{-1}, while the Fe^{2+}/Fe^{3+} contents increase to $4.5 \cdot 10^{-2}$ mol kg^{-1}, $14.3 \cdot 10^{-2}$ mol kg^{-1} and $15.7 \cdot 10^{-2}$ mol kg^{-1}, respectively. By comparison, it is found that with the increase of reaction time, iron powder proportion and water content, the Na^+ contents of Mt interlayer in degraded bentonite gradually decrease, while the Fe^{2+}/Fe^{3+} contents increase, suggesting that part of Na^+ in Mt interlayer are substituted by Fe^{2+}/Fe^{3+}.

Composition and structure of bentonite

The interlayer spacing of Mt is determined by the interplanar spacing d_{001}-value of the strongest basal plane (001) diffraction. Therefore, the diffraction peak of Mt (001) crystal plane is usually used as the characteristic peak of Mt[51,52]. Figure 3 shows the diffraction peak position (2θ) of Mt (001) crystal plane in the original GMZ Na-bentonite and degraded bentonite (B100_I1_W15, B100_I1_W30, B1_I1_W15 and B1_I1_W30 samples reacted for 90 days, and after removal of the iron powder/iron corrosion products) are 5.87°, 6.07°, 6.11°, 6.26° and 6.56°, respectively. Based on the Bragg equation: $2d\sin\theta = \lambda$ ($\lambda = 0.15406$ nm), the interlayer spacing (d) values of Mt in the above bentonite samples are 1.50 nm, 1.45 nm, 1.44 nm, 1.41 nm and 1.35 nm, respectively. This shows that in the reaction process of bentonite/iron powder, the interlayer spacing of Mt gradually decreases with the increase of water content and iron powder proportion. Furthermore, the intensity of the Mt diffraction peak decreases and the peak broadens, which may be caused by the
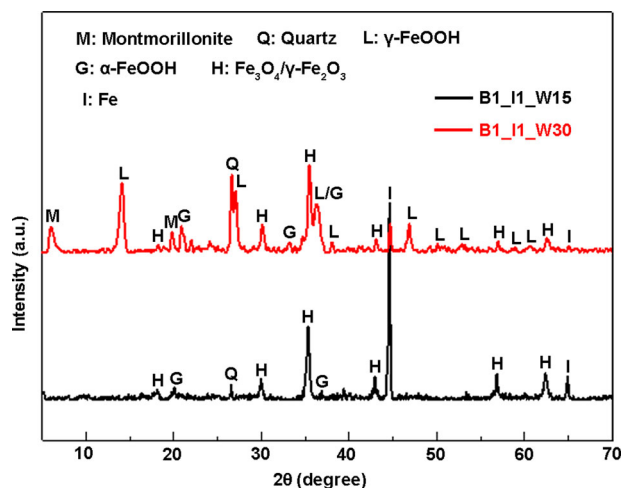
Fig. 1 XRD patterns of corrosion products of B1_I1_W15 and B1_I1_W30 samples reacted for 90 days.

Table 1. CEC of Mt interlayers in different bentonite samples.

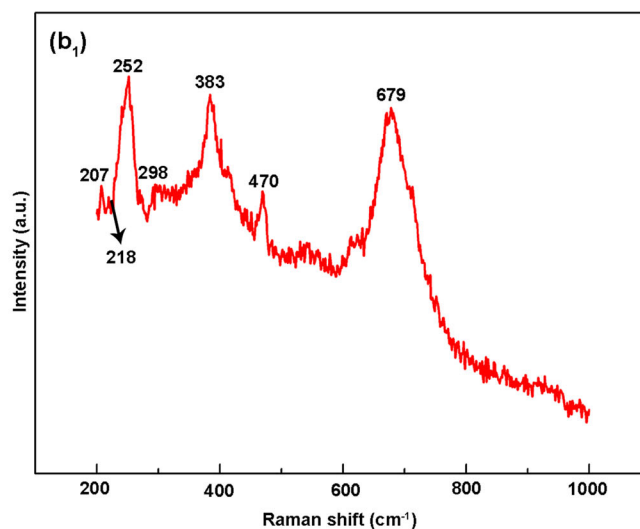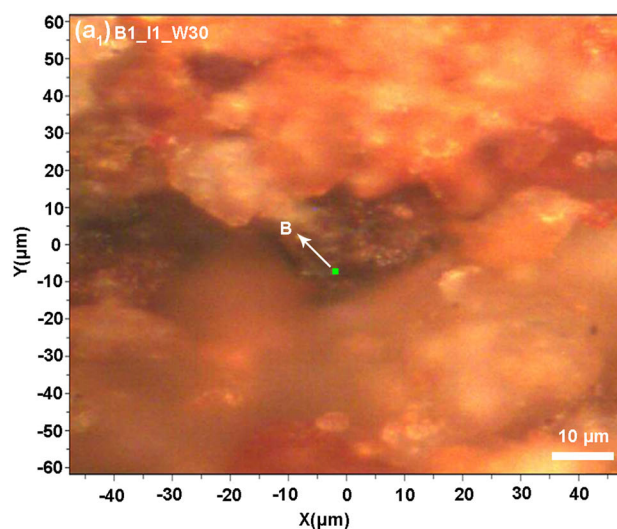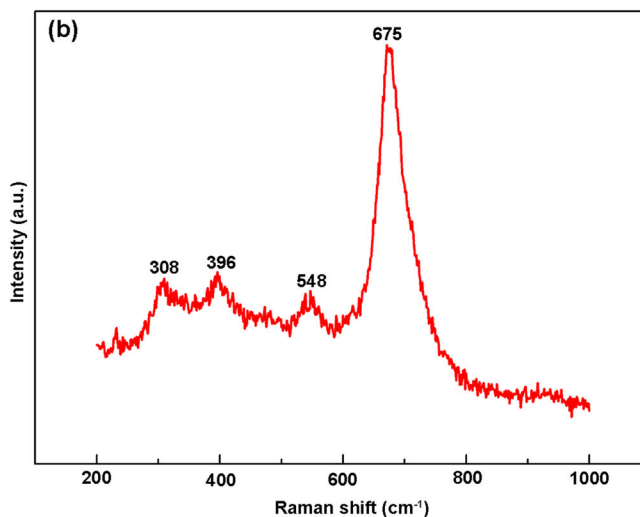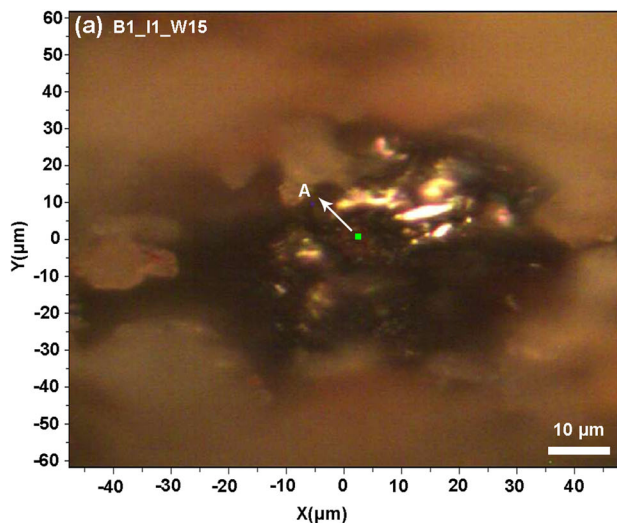| Time (days)	Samples	Water content (%)	Na^+ (10^{-2} mol/kg)	Fe^{2+}/Fe^{3+} (10^{-2} mol/kg)
	GMZ Na-bentonite	-	43.7	0.2
30	Bentonite : Iron powder = 100:1	15%	43.2	0.2
		30%	42.1	0.9
	Bentonite : Iron powder = 1:1	15%	41.5	1.2
		30%	35.2	4.5
60	Bentonite : Iron powder = 100:1	15%	41.9	0.9
		30%	39.4	2.6
	Bentonite : Iron powder = 1:1	15%	25.7	9.9
		30%	18.1	14.3
90	Bentonite : Iron powder = 100:1	15%	41.5	1.3
		30%	37.5	3.2
	Bentonite : Iron powder = 1:1	15%	24.3	10.7
		30%	16.2	15.7

Fig. 2 Macro-morphology and corrosion product analysis of B1_I1_W15 and B1_I1_W30 samples reacted for 90 days. **a** Macromorphology, **b** Raman spectrum of Point A and B.
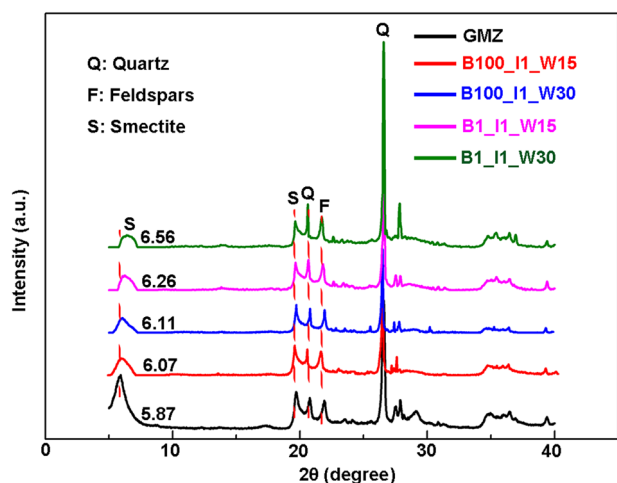
Fig. 3 XRD patterns of original GMZ Na-bentonite and degraded bentonite (B100_I1_W15, B100_I1_W30, B1_I1_W15, and B1_I1_W30 samples reacted for 90 days, and after removal of the iron powder/iron corrosion products).

Fig. 4 FTIR patterns of original GMZ Na-bentonite and degraded bentonite (B100_I1_W15, B100_I1_W30, B1_I1_W15, and B1_I1_W30 samples reacted for 90 days, and after removal of the iron powder/iron corrosion products).

decrease of Mt crystallinity[53,54]. To further understand the influence of iron corrosion products on the structure of Mt, the FITR spectra of original GMZ bentonite and degraded bentonite were performed.

Figure 4 shows the FTIR spectra of original GMZ Na-bentonite and degraded bentonite (B100_I1_W15, B100_I1_W30, B1_I1_W15 and B1_I1_W30 samples reacted for 90 days, an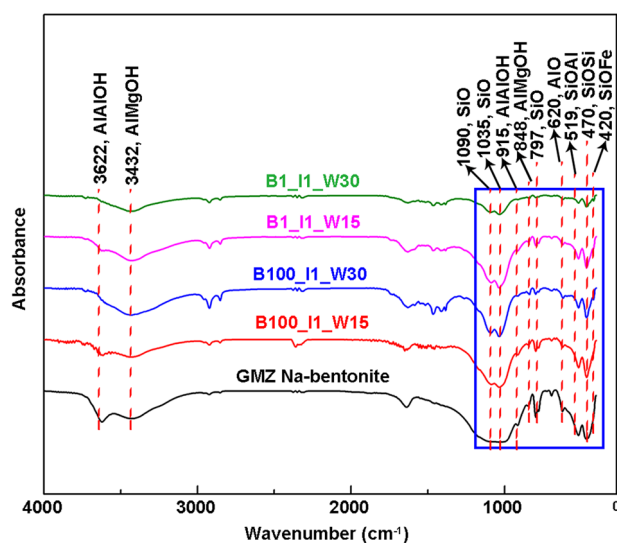d after removal of the iron powder/iron corrosion products). The obvious differences between FTIR spectra of degraded bentonite and original GMZ Na-bentonite are mainly manifested in the regions of absorption bands related to the vibrations of the octahedral ions. In the functional group region (4000–1330 cm^{-1}), the intensity of AlAlOH (~3622 cm^{-1}) stretching band in degraded bentonite exhibits a significant decrease, while that of AlMgOH (~3432 cm^{-1}) stretching band only shows a slight decrease[25].This may be related to the deprotonation of OH groups and partial collapse or destruction of Mt octahedral structure[25,26]. In the fingerprint region (1330–400 cm^{-1}), the variation of the stretching band intensities of AlAlOH (~915 cm^{-1}) and AlMgOH (~848 cm^{-1}) are consistent with those of the functional groups region[25,26]. Meanwhile, the intensities of bending bands of Si-O (~1090 cm^{-1}, ~1035 cm^{-1}, ~797 cm^{-1}), Al-O (~620 cm^{-1}), Si-O-Al (~519 cm^{-1}) and Si-O-Si (~470 cm^{-1}) are also decreased, which can be attributed to the partial dissolution or destruction of the Mt layer[25]. It can also be found that with the increase of water content and iron powder proportion, the intensities of these stretching bands and bending bands decrease, indicating that the deprotonation reaction of OH groups of Mt and the degree of dissolution or destruction of Mt structure are aggravated. Furthermore, a Si-O-Fe bending band is detected at the wavelength of 420 cm^{-1} of the FTIR spectra in degraded bentonite samples in Fig. 4, suggesting that Fe-containing silicate was generated, which may be composed of Fe^{2+}/Fe^{3+} adsorbed on the surface of Mt and Si-O- in Mt structure.

Figure 5a shows the TEM picture of the dry original GMZ Na-bentonite, and its main mineral component-Mt has a lamellar structure with a layer spacing value of 0.96 nm. Electron diffraction shows that the sample is in the [001] direction. Figure 5b and c show the TEM pictures of original GMZ Na-bentonite and degraded bentonite (B100_I1_W30 sample reacted for 90 days, and after removal of the iron powder/iron corrosion products) dispersed with water and acetone, respectively. It can be seen that the lamellar structure of Mt in the original GMZ Na-bentonite is intact, and the layer spacing value is 1.10 nm, which demonstrates that the layer spacing value of Mt increases after GMZ Na-bentonite is dispersed by water and acetone. The overall structure of Mt in degraded bentonite did not undergo any fundamental transformation, but as shown in the red dotted area in Fig. 5c, the edge of Mt sheet collapses,
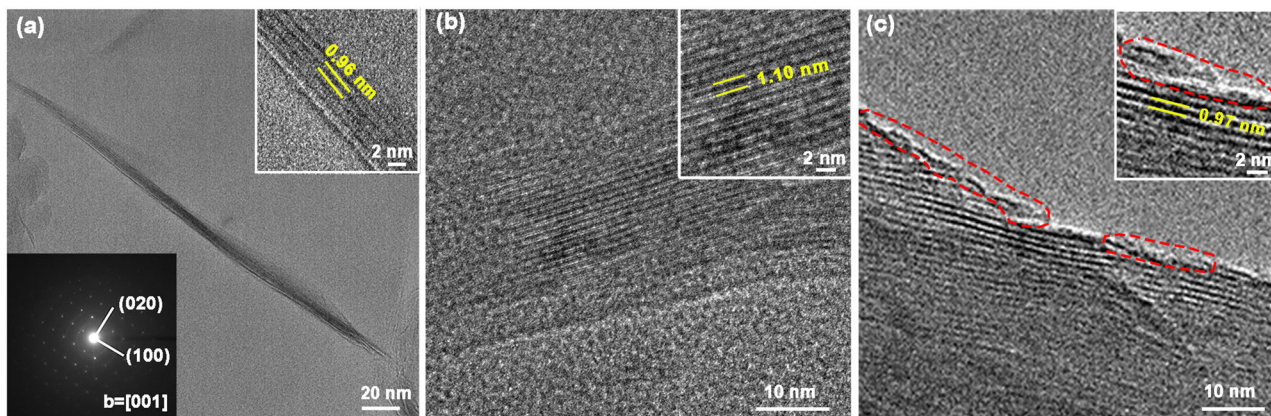

Fig. 5 TEM pictures. Dry original GMZ Na-bentonite (**a**), original GMZ Na-bentonite and dispersed with water and acetone (**b**) and the degraded bentonite (B100_I1_W30 sample reacted for 90 days, and after removal of the iron powder/iron corrosion products) dispersed with water and acetone (**c**).
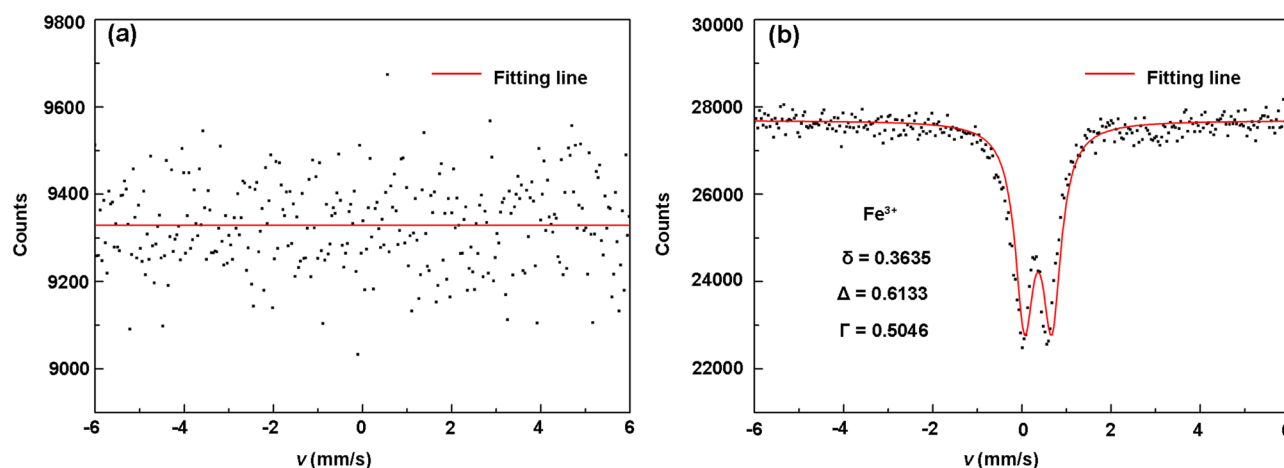
Fig. 6 ^{57}Fe Mössbauer spectra. Original GMZ Na-bentonite (**a**) and degraded bentonite-B1_I1_W30 sample reacted for 90 days, and after removal of the iron powder/iron corrosion products (**b**).

meaning that the edge structure of Mt is partially destroyed. In addition, compared with the original GMZ Na-bentonite, the layer spacing value of Mt in degraded bentonite is 0.97 nm, which further confirms that the layer spacing of Mt decreases after the bentonite was degraded.

Occurrence state of iron in Mt

Figure 6 shows the ^{57}Fe Mössbauer spectra of original GMZ Na-bentonite and degraded bentonite (B1_I1_W30 sample reacted for 90 days, and after removal of the iron powder/iron corrosion products). Based on the CEC measurement results of Mt interlayers in Table 1, it can be calculated that the iron ions content in original GMZ Na-bentonite is only 0.01%, far lower than the detection level of Mössbauer spectrum[31]. Therefore, the obtained resonance of ^{57}Fe Mössbauer spectrum in Fig. 6a is disordered. The Mössbauer spectrum can unambiguously differentiate the chemical states of Fe^{2+} and Fe^{3+}[29]. For the degraded bentonite, the experimental Mössbauer spectrum in Fig. 6b shows the typical broad Fe^{3+} resonance observed for most Mts, and the intensities of the component peaks of this resonance are definitely asymmetric[55].

Generally speaking, the Mössbauer spectra of iron oxides and hydroxides usually consists of six magnetic splitting lines[30]. However, there is no discernible six magnetic splitting lines in Fig. 6b. Meanwhile, the phases of iron, iron oxides and hydroxides were not detected in the corresponding XRD patterns of degraded bentonite in Fig. 3. Therefore, it is certain that Fe^{3+} in the degraded bentonite either enters Mt interlayer or Al-O octahedral sites. If Fe^{3+} occupies the Al-O octahedral sites, the saturation coordination number around Fe should be 6, the symmetry is very high, and the electric quadrupole splitting value (Δ) should be very small. However, the Δ value of Fe^{3+} in Fig. 6b is large, indicating that the partial charge of Fe is incompletely balanced by the (number of) attached ligands. Thence, the Fe^{3+} is more likely to be adsorbed on the surface of Mt laminate and enter the Mt interlayer[29,30]. This is consistent with TEM and XRD results that the interlayer spacing of Mt decreases after bentonite/iron powder reaction. Furthermore, the in-layer diffusion of divalent cations (as demonstrated for Ni^{2+}) into the clay octahedral sheet (the so-called Hofmann-Klemen) is not expected to occur below 50 °C[56]. The Ni^{2+} is similar to Fe^{2+}/Fe^{3+} in terms of ionic radius and affinity towards the clay structure[57,58], and the experiments were performed at ambient temperatures, which further confirms that iron ions generated by iron corrosion mainly enters the interlayer domain of Mt.

Water absorption and swelling performance of bentonite

Figure 7 shows the time-history curves of constant volume swelling force of compacted samples of original GMZ Na-bentonite (1#), original bentonite/iron powder (B100_I1 2#, B10_I1 5#, B1_I1 8#) and their reacted at 15%, 30% water content (B100_I1_W15 3#, B100_I1_W30 4#, B10_I1_W15 6#, B100_I1_W30 7#, B1_I1_W15 9#, B1_I1_W30 10#) for 90 days. It can be seen that the time-history curves of swelling force of the 1–3# samples present a typical double-peak characteristic[59], that is, the swelling force of the sample rapidly increases after absorbing water, decreases slightly after reaching the peak value, then increases again, and finally tends to be stable. However, the time-history curves of swelling force of 4–10# samples show a typical single-peak characteristic, that is, the swelling force of the sample increases rapidly after absorbing water, then gradually decreases after reaching the peak value, and finally becomes stable. The evolution process of swelling force of bentonite and bentonite/iron powder (before and after degradation) under the condition of constant volume is essentially the accumulation process of "wedge" force formed between crystal layers and laminates due to the restriction of the thickening process of the bonding water film between crystal layers and the diffuse double electric layer between laminates[60]. This accumulated "wedge" force will decrease due to the crack of the laminates and the collapse of the pores between the aggregates and then increase again with the continued water absorption and swelling of the cracked laminates[61]. Macroscopically, it shows the double-peak or single-peak shape of the time-history curve of swelling force. Therefore, the swelling force can be regarded as the superposition result of the accumulated "wedge" force Ps^+ caused by the swelling of the crystal layer and the electric double layer and the dissipated "wedge" force Ps^- caused by the lamination cracking and the pore collapse between aggregates[62].

Table 2 shows the swelling force parameters of 1–10# samples in the process of water absorption. It can be found that the peak value, final value and the time required to reach the peak value of the original GMZ Na-bentonite (1#) are higher than those of the bentonite/iron powder samples (2–10#). This can be attributed to the higher bentonite content and better swelling capacity of the original GMZ Na-bentonite compacted sample. Also, it has not been degraded by iron corrosion products and has better colloidal stability and swelling capacity. For the samples containing iron powder with different proportions (2–4#, 5–7#, 8–10#), the peak value, the final value and the time needed to reach the peak value of swelling force all decrease whether before or after degradation of bentonite. Based on the results in sections 2.2–2.4, the reasons for the decrease of the swelling performance of degraded
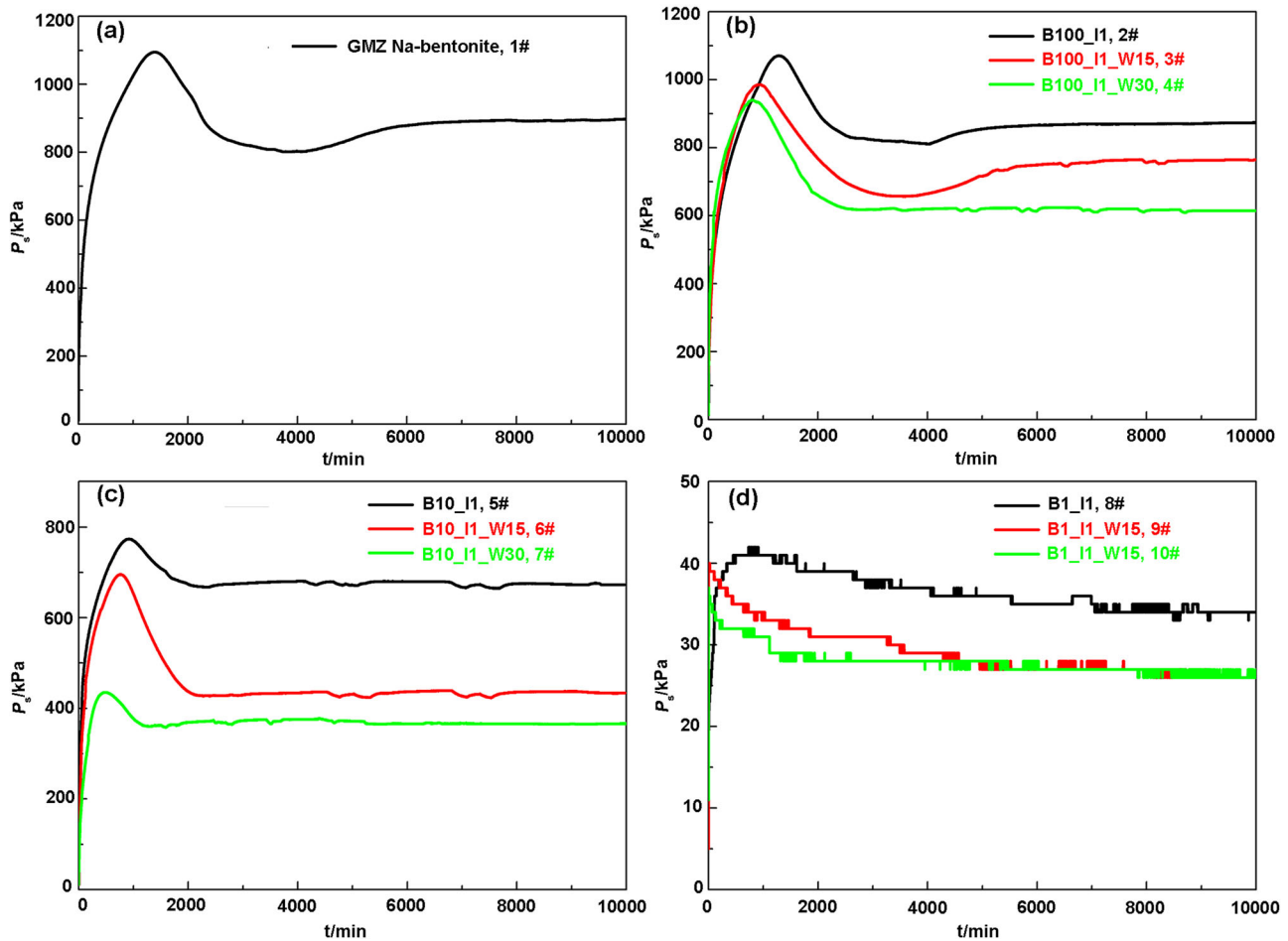
Fig. 7 Time-history curves of swelling force of compacted samples. Original GMZ Na-bentonite (**a**), original bentonite/iron powder (100:1 (**b**), 10:1 (**c**), 1:1 (**d**)) and their reacted at 15%, 30% water content for 90 days.

No	Samples	Preparation conditions	Peak swelling force (kPa)	Time (min)	Final swelling force (kPa)
1#	GMZ Na-bentonite	Original	1095	1388	897
2#	Bentonite : iron power = 100:1	Original	1071	1283	873
3#		15% water content, 90 days	985	931	764
4#		30% water content, 90 days	941	798	614
5#	Bentonite : iron power = 10:1	Original	774	916	673
6#		15% water content, 90 days	696	770	434
7#		30% water content, 90 days	435	483	366
8#	Bentonite : iron power = 1:1	Original	42	812	34
9#		15% water content, 90 days	40	15	26
10#		30% water content, 90 days	37	5	26

Table 2. Swelling force parameters of different bentonite compacted samples in the process of water absorption.

bentonite can be summarized as follows: (1) The Fe^{2+}/Fe^{3+} produced by iron corrosion migrate to Mt crystal layer and substitute Na^+, which leads to the decrease of cation hydration ability and interlayer spacing[53]. (2) The destruction of the Mt structural integrity can cause the decrease of Mt content in bentonite. (3) The adsorption of Fe^{2+}/Fe^{3+} on the surface of Mt laminate can neutralize the negative charge of Mt, thus reducing the repulsive force of the diffused electric double layer on the surface of the laminate[16]. Furthermore, with the decrease of bentonite swelling force and the formation of iron corrosion

products, the porosity and permeability of bentonite increase, and the time needed to reach the peak value of swelling force is shortened.

Figure 8 shows the water absorption after wetting for 10,000 min of 1–10 # compacted samples. It can be seen that the water absorption (wt.%) of the original GMZ Na-bentonite compacted sample (1#) is 31.03%, which is higher than that of bentonite/iron powder samples (2–10#). This can be attributed to the high Mt content, large interlayer spacing and strong water absorption capacity of the original GMZ Na-bentonite. For 100:1
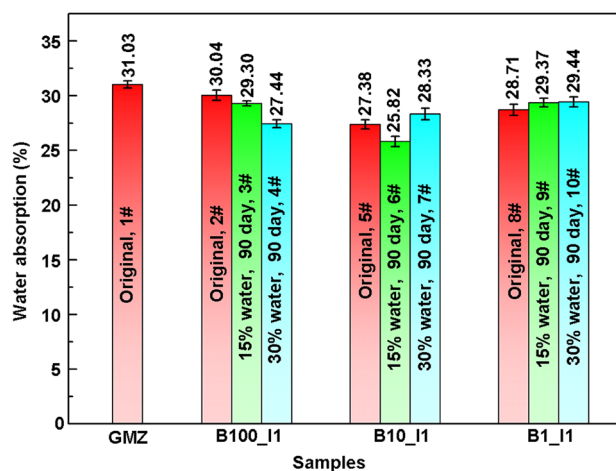
Fig. 8 Water absorption after wetting for 10,000 min of compacted samples of original GMZ Na-bentonite, original bentonite/iron powder (100:1, 10:1, 1:1) and their reacted at 15%, 30% water content for 90 days.

bentonite/iron powder, the water absorption of 2–4# samples gradually decreases as follows: 30.04%, 29.30% and 27.44%, respectively. This is mainly related to the decrease of water absorption capacity of bentonite caused by the decrease of Mt content, lamination volume and interlayer spacing. Meanwhile, the pores between bentonite aggregates increases, which leads to the increase of free water entering bentonite[62]. Therefore, the water absorption of the sample ultimately depends on its water absorption capacity and pores between aggregates. For 10:1 bentonite/iron powder, the water absorption of 5# and 6# samples are 27.38% and 25.82% respectively, showing a decreasing trend, which is similar to those of 2–4# samples. Compared with 5# and 6# samples, the water absorption rate of 7# sample increases to 28.33%, indicated that water absorption of 7# sample is mainly affected by the increase of pores between aggregates. For 1:1 bentonite/iron powder, the water absorption of 8–10# samples gradually increases as follows: 28.71%, 29.37% and 29.44%, respectively, which is similar to that of 7# sample. In addition, the existence of iron powder and iron corrosion products can also increase the porosity of the sample and has a great influence on its water absorption.

Degradation mechanism of Mt structure

As the main mineral component of bentonite, the variations in Mt structure and physicochemical properties are the key factors affecting the buffering barrier performance of bentonite. In mildly acidic (aerated) conditions, the protons in the solution are abundant, thus Mt does not participate directly in the corrosion of metallic iron[26]. However, under alkaline conditions, protons mainly exist in Mt structure with the form of OH groups, and deprotonation can occur at both Mt interlayer and edge sites. Therefore, in the weak alkaline environment of simulated Beishan groundwater (pH = 8.15), the deprotonation of OH groups in Mt structure is very likely to participate in the corrosion process of iron-based containers for HLW disposal. It has been recognized that the high affinity of metallic iron for Mt and the resulting interaction are the causes of steel pipe corrosion when using clay-containing drilling fluid[63]. The presence of metallic iron can induce deprotonation of OH groups of octahedral Mt, while metallic iron loses electrons and further corrodes. Therefore, with the passage of time, the metallic iron is continuously corroded, and Mt is gradually degraded.

For the degraded bentonite, the intensities of AlAlOH and AlMgOH stretching bands in FTIR decrease, illustrating that the

OH group in Mt structure participated in deprotonation reaction[25]. Moreover, the formation of Si-O-Fe bending band and the results of CEC, Mössbauer spectrum, XRD, TEM further indicate that Fe^{2+}/Fe^{3+} generated by iron corrosion mainly entered the interlayer domain of Mt (directly or through substitution with interlayer low-valent cations). Therefore, as shown in Fig. 9, a conceptual model of Mt structure destabilization and degradation is put forward: (a) The activity of reduced iron powder can promote the deprotonation of OH group of octahedral Mt, and pH increase, which further accelerated the ionization of AlAlOH and AlMgOH, release H^+ to form $AlAlO^-$ and $AlMgO^-$. Meanwhile, Fe^{2+}/Fe^{3+} is dissolved from metal iron corrosion. (b) The formation of $AlAlO^-$ and $AlMgO^-$ causes Fe^{2+}/Fe^{3+} to be adsorbed on the surface of the Mt laminate and further enter into the Mt crystal layer (directly or through substitution with interlayer low-valent cations) to compensate for the interlayer charge deficit. (c) With time, the metallic iron is continuously dissolved, the amount of Fe^{2+}/Fe^{3+} entering the Mt structure increases, and the Mt interlayer spacing gradually decreases.

In summary, the microstructure analysis shows that Fe^{2+}/Fe^{3+} dissolved from the reduced iron powder could adsorbed on the surface of montmorillonite (Mt) laminate and substituted part of Na^+ in Mt interlayer, which caused the decrease of the volume and interlayer spacing of Mt. Meanwhile, the structural integrity of Mt in bentonite was destroyed. In terms of macroscopic properties, Fe^{2+}/Fe^{3+} generated by iron corrosion significantly decreased the water absorption and swelling capacity of bentonite. Furthermore, the degradation of bentonite structure and properties was aggravated with the increase of iron powder proportion, water content and reaction time. The destabilization and degradation mechanism of Mt structure in bentonite was put forward: Fe^{2+}/Fe^{3+} generated by iron corrosion entered the interlayer domain of Mt (directly or through substitution with interlayer low-valent cations) to compensate the interlayer charge deficit.

METHODS

Sample preparation

The mineral composition of GMZ Na-bentonite in Inner Mongolia is: montmorillonite, $75 \pm 1\%$; quartz, $12 \pm 1\%$; cristobalite, $7 \pm 1\%$; feldspar, $4 \pm 1\%$; kaolinite, $1 \pm 1\%$; calcite, $1 \pm 1\%$[64]. Before the experiment, the bentonite powder was dried in an oven at $105 \pm 3 \,°C$ (under ambient conditions) for 8 hours to remove the naturally absorbed water in the bentonite. The simulated Beishan groundwater solution was prepared under aerobic conditions according to the groundwater sample composition of BS03 well in the old well section of Beishan area[49], and the specific components are given as follows: $NaSO_4$, $1.5777 \, g \, L^{-1}$; NaCl, $1.4876 \, g \, L^{-1}$; $CaCl_2$, $0.5792 \, g \, L^{-1}$; $MgSO_4 \cdot 7H_2O$, $0.5716 \, g \, L^{-1}$; $NaHCO_3$, $0.1384 \, g \, L^{-1}$; $NaNO_3$, $0.0372 \, g \, L^{-1}$; KCl, $0.0382 \, g \, L^{-1}$.

The prepared simulated solution was frozen at $-40 \,°C$, crushed by an ice crusher, and sieved to obtain ultrafine ice powder with a particle size of $<10 \, \mu m$. In order to explore the influence of the corrosion degree of iron-based containers on the structure and properties of bentonite, iron powder, bentonite and ice powder were thoroughly mixed and stirred in different proportions (see Table 3) at the low temperature of $-40 \,°C$, then vacuum sealed and reacted at room temperature. Through the analysis of iron corrosion products, combined with the parameters variations of Mt interlayer exchangeable cation content, mineral composition, interlayer spacing, occurrence state of iron in Mt, water absorption and swelling capacity to reveal the mechanism of degradation of Mt structure.

The preparation process of iron corrosion products/degraded bentonite for XRD analysis (idem for the other techniques) was as follows: (1) B1_I1_W15 and B1_I1_W30 samples reacted for
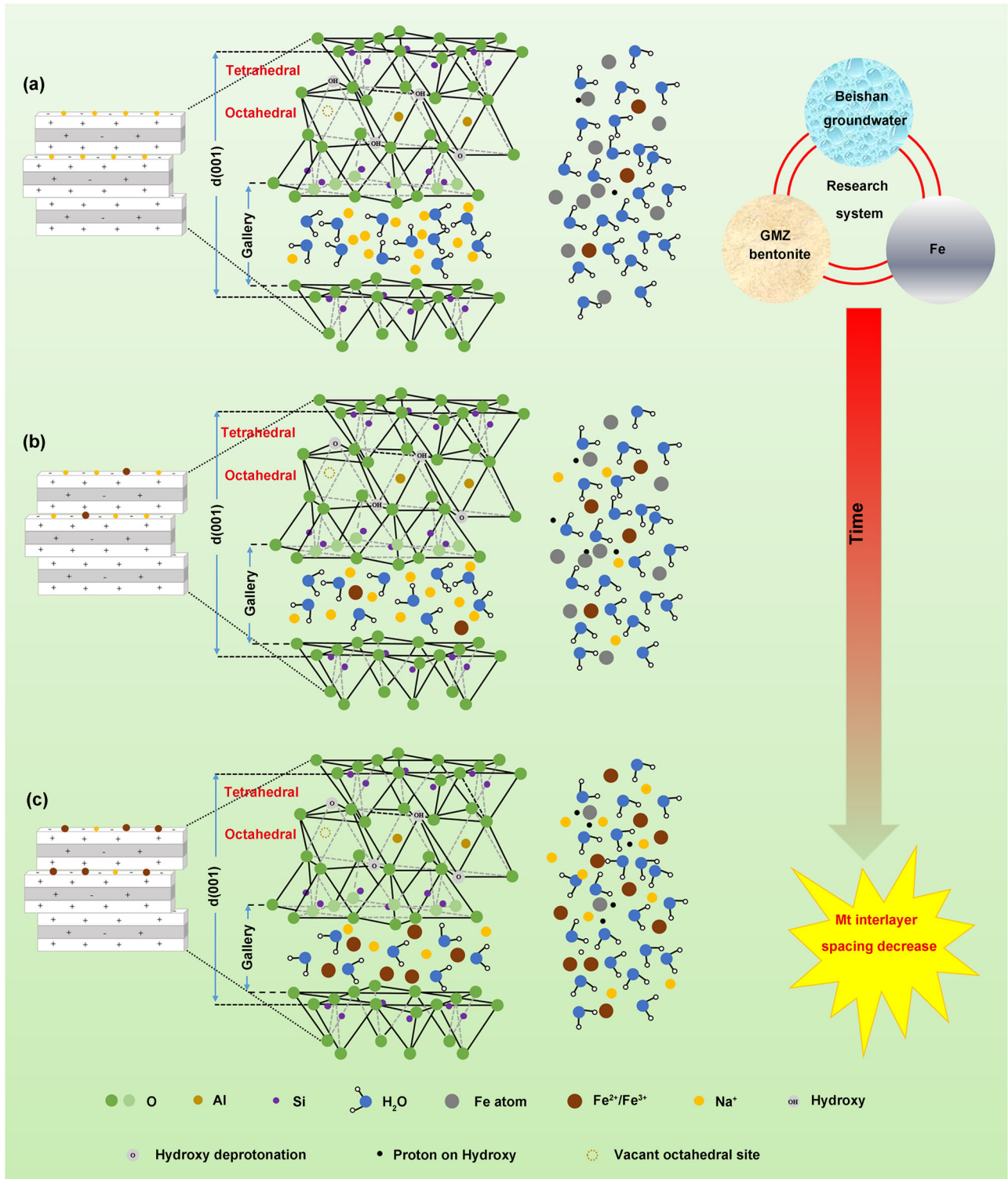
Fig. 9 Conceptual model of Mt structural degradation. a AlAlOH and AlMgOH ionize and release H^+ to form $AlAlO^-$ and $AlMgO^-$, **b** Fe^{2+}/Fe^{3+} mainly enter into the Mt interlayer to compensate for the interlayer charge deficit. **c** With time, the amount of Fe^{2+}/Fe^{3+} entering the Mt structure increases, and the Mt interlayer spacing gradually decreases.

90 days under sealed anoxic conditions; (2) The mixed samples after the reaction were put in a glove box, dried with high purity nitrogen (>99.999%), grounded, sieved and vacuum sealed; (3) The iron powder/iron corrosion products and degraded bentonite were separated from the mixed samples by a strong-field magnet.

Analysis of iron corrosion products
X-ray diffraction (XRD, Cu-K-alpha, Smartlab 9 kW, Rigaku, Japan) and Raman spectroscopy (HR800, Horiba Jobin-Yvon, France) were used to characterize the phase composition of the iron corrosion products. The XRD test was carried out with Cu ka ($\lambda = 0.15406$ nm) at 50 kv-250 mA, and the scanning range and

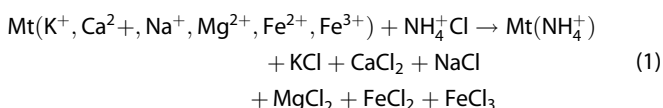**Table 3.** Compositions proportion of bentonite/iron powder mixed samples.

Bentonite : Iron powder	Water content (%)	Ice powder (g)	Bentonite (g)	Iron powder (g)
100:1	15	17.65	100	1
	30	42.88	100	1
10:1	15	17.65	100	10
	30	42.88	100	10
1:1	15	17.65	100	100
	30	42.88	100	100

Table 4. Related parameters of different compacted bentonite sample preparation.

No.	Samples	Preparation conditions	Total weight (g)	Total Density (g/cm³)	Height (cm)
1#	GMZ Na-bentonite	Original	95.3	1.512	2.192
2#	Bentonite : Iron powder = 100:1	Original	95.8	1.517	2.196
3#		15% water content, 90 days	95.4	1.521	2.181
4#		30% water content, 90 days	96.3	1.534	2.184
5#	Bentonite : Iron powder = 10:1	Original	96.1	1.527	2.189
6#		15% water content, 90 days	95.9	1.534	2.175
7#		30% water content, 90 days	96.2	1.533	2.182
8#	Bentonite : Iron powder = 1:1	Original	96.2	1.575	2.124
9#		15% water content, 90 days	96.5	1.567	2.142
10#		30% water content, 90 days	96.3	1.568	2.136

speed were set at 5–70° and 10° min^{-1} respectively. The results were qualitatively analyzed by Jade 6.0 software. For the Raman spectrum analysis, a He-Ne light source with a wavelength of 632.8 nm was adopted as the laser beam, the spot size was 1 μm^2, and the objective used to focus the beam was x50LWD. In addition, the laser power was always kept below 1 mW to avoid the composition of corrosion products being changed by laser heating, and the accumulation time was 30 s. The results were qualitatively analyzed based on the published literatures[38–43].

CEC measurement of Mt interlayers in bentonite

To investigate the effect of Fe^{2+}/Fe^{3+} dissolved from iron corrosion on the CEC of Mt interlayers in GMZ Na-bentonite, Inductively coupled plasma emission spectroscopy (ICP-OES, iCAP 7000, Thermo Fisher, Singapore) was employed to measure the Na^+ and Fe^{2+}/Fe^{3+} content of Mt interlayer in original GMZ bentonite and degraded bentonite (B100_I1_W15, B100_I1_W30, B1_I1_W15 and B1_I1_W30 samples reacted for 30 days, 60 days and 90 days, and after removal of the iron powder/iron corrosion products). Before ICP-OES measurement, the bentonite was rinsed several times with deionized water under the anoxic condition in a glovebox to remove the salt solution adsorbed on the surface of the sample, and then dried with high-purity nitrogen, ground, sieved, and sealed for storage. The CEC in Mt interlayer was measured by the $NH_3·H_2O$-NH_4Cl method[65], and the reaction formula was given as follows:

$$Mt(K^+, Ca^{2+}, Na^+, Mg^{2+}, Fe^{2+}, Fe^{3+}) + NH_4^+Cl \rightarrow Mt(NH_4^+)$$
$$+ KCl + CaCl_2 + NaCl \qquad (1)$$
$$+ MgCl_2 + FeCl_2 + FeCl_3$$

Composition and structure analysis of bentonite

XRD was applied to analyze the mineral composition of the original GMZ Na-bentonite and degraded bentonite (B100_I1_W15, B100_I1_W30, B1_I1_W15 and B1_I1_W30 samples reacted for 90 days, and after removal of the iron powder/iron corrosion products). The XRD test was carried out with Cu ka (λ = 0.15406 nm) at 50 kv-250 mA, and the scanning range and speed were set at 5–40° and 10° min^{-1} respectively. The results were qualitatively analyzed by Jade 6.0 software.

Fourier transform infrared spectroscopy (FTIR, EQUINOX 55, Bruker, Europe) was employed to detect the chemical bonds and functional groups of bentonite molecular structure, and the transmittance was measured on KBr pressed-disc technique (1 mg of sample and 200 mg of KBr)[25,26]. For each sample, 16 scans were recorded with a resolution of 2 cm^{-1}. The measurement range of infrared wavelength was 4000–400 cm^{-1}, and the spectral manipulations were performed using the OMNIC software package[25].

Spherical-aberration-corrected transmission electron microscope (TEM, Titan G2 60–300, FEI, U.S.) was used to analyze the microstructure of Mt in the original GMZ Na-bentonite and degraded bentonite (B100_I1_W30 sample reacted for 90 days, and after removal of the iron powder/iron corrosion products). Before TEM measurement, the bentonite was dispersed in acetone solution at a ratio of 1:50, and then the sample was fished with a 230-mesh copper net. Furthermore, it is worth noting that the average thickness difference between TEM samples of Mt microcrystal was not affected by humidity[25,66,67].

The ^{57}Fe Mössbauer spectra of iron in Mt

The Mössbauer spectroscopy was used to characterize the occurrence state of iron in original GMZ Na-bentonite and degraded bentonite (B1_I1_W30 sample reacted for 90 days, and after removal of the iron powder/iron corrosion products). The Mössbauer spectrometer (^{57}Co (Rh) source, MFD-500AV, Topologic, Japan) was used to record ^{57}Fe Mössbauer spectra at room temperature (RT, 298 K). The velocity scale was calibrated with reference to α-Fe, with the midpoint of the iron hyperfine spectrum defining zero velocity. The data analysis and fitting of ^{57}Fe Mössbauer spectrum were carried out by Mosswinn 4.0 software. To eliminate the effects of absorber thickness, all the absorber samples contained 7–10 mg Fe cm^{-2} [29].

Measurement of water absorption and swelling performance

A self-developed bentonite compaction apparatus was employed to prepare compacted samples of original GMZ Na-bentonite and 100:1, 10:1 and 1:1 bentonite/iron powder (before/after degradation). Before sample preparation, the original bentonite powder was dried in an oven at 105 ± 3 °C (under ambient conditions) for 8 h. The reacted bentonite/iron powder mixed samples were dried with high purity nitrogen in a glove box at room temperature (under anoxic conditions) until the weight remained stable. Table 4 shows the relevant trial parameters of different compacted bentonite samples described above. The motor loading fully

automated-mechanical apparatus (YUC.YJZPZ-1, Yuchuang technology, China) was used for real-time monitoring of the constant volume swelling force of different compacted samples in the process of water absorption. The swelling force test adopted the loading mode of constant deformation, the running speed was $0.1 \, mm \, min^{-1}$, and the test period lasted for 10,000 min. The water absorption of compacted samples of original GMZ bentonite and bentonite/iron powder (before/after degradation) was calculated by the following formula:

$$Water \, absorption(\%) = \frac{W_1 - W_0}{W_0} \tag{2}$$

W_0 is the initial weight of sample, W_1 the weight of sample after water absorption.

DATA AVAILABILITY
The data that support the findings of this study are available from the corresponding authors upon reasonable request.

REFERENCES

1. Johnson, L. & King, F. The effect of the evolution of environmental conditions on the corrosion evolutionary path in a repository for spent fuel and high-level waste in opalinus clay. *J. Nucl. Mater.* **379**, 9–15 (2008).
2. Montes, H. G., Fritz, B., Clement, A. & Michau, N. Modelling of geochemical reactions and experimental cation exchange in MX 80 bentonite. *J. Environ. Manage.* **77**, 35–46 (2005).
3. Zhang, F., Ye, W., Wang, Q., Chen, Y. & Chen, B. An insight into the swelling pressure of GMZ01 bentonite with consideration of salt solution effects. *Eng. Geol.* **251**, 190–196 (2019).
4. Guo, X., Gin, S. & Frankel, G. S. Review of corrosion interactions between different materials relevant to disposal of high-level nuclear waste. *npj Mater. Degrad.* **4**, 34–50 (2020).
5. Smart, N. R., Reddy, B., Rance, A. P., Nixon, D. J. & Diomidis, N. The anaerobic corrosion of carbon steel in saturated compacted bentonite in the Swiss repository concept. *Corros. Eng., Sci. Technol.* **52**, 113–126 (2017).
6. Zhang, Z., Ye, W., Liu, Z., Wang, Q. & Cui, Y. Mechanical behavior of GMZ bentonite pellet mixtures over a wide suction range. *Eng. Geol.* **264**, 105383–105391 (2020).
7. Xu, L., Ye, W., Chen, B., Chen, Y. & Cui, Y. Experimental investigations on thermo-hydro-mechanical properties of compacted GMZ01 bentonite-sand mixture using as buffer materials. *Eng. Geol.* **213**, 46–54 (2016).
8. Lee, J. O., Lim, J. G., Kang, I. M. & Kwon, S. Swelling pressures of compacted Ca-bentonite. *Eng. Geol.* **129–130**, 20–26 (2012).
9. Wang, Q., Meng, Y., Su, W., Ye, W. & Chen, Y. Cracking and sealing behavior of the compacted bentonite upon technological voids filling. *Eng. Geol.* **292**, 106244–106255 (2021).
10. Wei, X. et al. Study on corrosion behavior of low carbon steel under different water conditions in bentonite of China-Mock-Up. *Appl. Clay Sci.* **167**, 23–32 (2019).
11. Cui, S., Zhang, H. & Zhang, M. Swelling characteristics of compacted GMZ bentonite–sand mixtures as a buffer/backfill material in China. *Eng. Geol.* **141-142**, 65–73 (2012).
12. Sun, D., Zhang, J., Zhang, J. & Zhang, L. Swelling characteristics of GMZ bentonite and its mixtures with sand. *Appl. Clay Sci.* **83–84**, 224–230 (2013).
13. He, H., Ma, Y., Zhu, J., Peng, Y. & Qing, Y. Organoclays prepared from montmorillonites with different cation exchange capacity and surfactant configuration. *Appl. Clay Sci.* **48**, 67–72 (2010).
14. Ye, W., Chen, Y., Bao, C., Wang, Q. & Ju, W. Advances on the knowledge of the buffer/backfill properties of heavily-compacted GMZ bentonite. *Eng. Geol.* **116**, 12–20 (2010).
15. Bergaya, F., Theng, B. K. G. & Lagaly, G. Developments in clay science. *Handbook of Clay Science* **1**, 1224 (2006).
16. Egloffstein, T. A. Natural bentonites-influence of the ion exchange and partial desiccation on permeability and self-healing capacity of bentonites used in GCLs. *Geotext. Geomembranes* **19**, 427–444 (2001).
17. Ramirez, S., Cuevas, J., Vigil, R. & Leguey, S. Hydrothermal alteration of "La Serrata" bentonite (Almeria, Spain) by alkaline solutions. *Appl. Clay Sci.* **21**, 257–269 (2002).
18. Karnland, O., Olsson, S., Nilsson, U. & Sellin, P. Experimentally determined swelling pressures and geochemical interactions of compacted Wyoming bentonite with highly alkaline solutions. *Phys. Chem. Earth* **32**, 275–286 (2007).
19. Fernández, R., Cuevas, J. & Mäder, U. K. Modeling experimental results of diffusion of alkaline solutions through a compacted bentonite barrier. *Cem. Concr. Res.* **40**, 1255–1264 (2010).
20. Chen, B., Zhang, H. & Chen, P. Influence of hyper-alkaline solution infiltration on microscopic pore structure of compacted GMZ bentonite. *J. Zhejiang Univ. (Eng. Sci.)* **47**, 602–608 (2013).
21. Zahrim, A. Y. et al. Nanoparticles enhanced coagulation of biologically digested leachate. *Nanotechnol. Water Wastewater Treat*. 205–241. https://doi.org/10.1016/B978-0-12-813902-8.00011-3 (2019).
22. Carlson, L. et al. Experimental studies of the interactions between anaerobically corroding iron and bentonite. *Phys. Chem. Earth* **32**, 334–345 (2007).
23. Bennett, D. G. & Gens, R. Overview of European concepts for high-level waste and spent fuel disposal with special reference waste container corrosion. *J. Nucl. Mater.* **379**, 1–8 (2008).
24. Kaufhold, S., Hassel, A. W., Sanders, D. & Dohrmann, R. Corrosion of high-level radioactive waste iron-canisters in contact with bentonite. *J. Nucl. Mater.* **285**, 464–473 (2015).
25. Osacky, M., Sucha, V., Czimerova, A. & Madejova, J. Reaction of smectites with iron in a nitrogen atmosphere at 75 °C. *Appl. Clay Sci.* **50**, 237–244 (2010).
26. Lantenois, S., Lanson, B., Muller, F., Bauer, A. & Planon, A. Experimental study of smectite interaction with metal Fe at low temperature, 1. Smectite destabilization. *Clays Clay Miner.* **53**, 597–612 (2005).
27. Perronnet, M. et al. Towards a link between the energetic heterogeneities of the edge faces of smectites and their stability in a context of metallic corrosion. *Geochim. Cosmochim. Acta* **71**, 1463–1479 (2007).
28. Helsen, J. A. Characterization of Iron(II)-and Iron(III)-exchanged montmorillonite and hectorite using the Mössbauer effect. *Clay Miner.* **18**, 117–125 (1983).
29. Diamant, A. & Pasternak, M. Characterization of adsorbed iron in montmorillonite by Mössbauer spectroscopy. *Clays Clay Miner.* **30**, 63–66 (1982).
30. Bartonkova, H. et al. Mössbauer study of iron oxide modified montmorillonite. *Hyperfine Interact* **165**, 221–225 (2005).
31. Johnston, J. H. Iron substitution in montmorillonite, Illite, and Glauconite by ^{57}Fe Mössbauer spectroscopy. *Clays Clay Miner.* **35**, 170–176 (1987).
32. Heller-Kallai, L. & Rozenson, I. The use of mössbauer spectroscopy of iron in clay mineralogy. *Phys. Chem. Miner.* **7**, 223–238 (1981).
33. Gracia, M., Gancedo, J. R., Marco, J. F., Franco, M. J. & Pajares, J. A. Mössbauer study of iron removal in a montmorillonite. *Hyperfine Interact* **46**, 629–634 (1989).
34. Lounis, Z., Saddouki, S. & Djafri, F. Removal of Pb^{2+} ions in aqueous phase by a sodic Montmorillonite. *J. Anal. Sci. Technol.* **3**, 104–112 (2012).
35. Xian, Z., Hao, Y., Bai, H., Zhao, Y. & Song, S. Correlation of montmorillonite exfoliation with interlayer cations in the preparation of two-dimensional nanosheets. *RSC Adv.* **7**, 41471–41478 (2017).
36. Wei, X., Dong, J., Chen, N., Yadav, A. P. & Ke, W. Effects of bentonite content on the corrosion evolution of low carbon steel in simulated geological disposal environment. *J. Mater. Sci. Technol.* **66**, 45–56 (2020).
37. Zhang, C. et al. Novel Insights into the hydroxylation behaviors of α-Quartz (101) surface and its effects on the adsorption of sodium oleate. *Minerals* **9**, 450–468 (2019).
38. Dunnwald, J. & Otto, A. An investigation of phase transitons in rust layers using raman spectroscopy. *Corros. Sci.* **29**, 1167–1176 (1989).
39. DeFaria, D. L. A., Silva, S. V. & DeOliveira, M. T. Raman microspectroscopy of some iron oxides and oxyhydroxides. *J. Raman Spectrosc.* **28**, 873–878 (1997).
40. Verble, J. L. Temperature-dependent light-scattering studies of the Verwey transition and electronic disorder in magnetite. *Phys. Rev. B* **9**, 5236–5248 (1974).
41. Oh, S. J., Cook, D. C. & Townsend, H. E. Characterization of iron oxides commonly formed as corrosion products on steel. *Hyperfine Interact.* **112**, 59–65 (1998).
42. Ohtsuka, T. & Tanaka, S. Monitoring the development of rust layers on weathering steel using in situ Raman spectroscopy under wet-and-dry cyclic conditions. *J. Solid State Electrochem.* **19**, 3559–3566 (2015).
43. Hart, T. R. et al. *Proceedings of the 3rd international conference on light scattering in solids, flammarion, Paris.* 254–258 (1976).
44. Refait, P., Benali, O., Abdelmoula, M. & Genin, J. M. R. Formation of 'ferric green rust' and/or ferrihydrite by fast oxidation of iron(II–III) hydroxychloride green rust. *Corros. Sci.* **45**, 2435–2449 (2003).
45. Xue, F. et al. Effect of residual dissolved oxygen on the corrosion behavior of low carbon steel in 0.1 M $NaHCO_3$ solution. *J. Mater. Sci. Technol.* **34**, 1349–1358 (2018).
46. Wei, X. et al. Influence of deteriorated bentonite sediments on the corrosion behavior of NiCu low alloy steel. *Acta Metall. Sin. (Engl. Lett.)* **35**, 1011–1022 (2021).

47. Wei, X. et al. Effects of aerobic and anoxic conditions on the corrosion behavior of NiCu low alloy steel in the simulated groundwater solutions. *Acta Metall. Sin. (Engl. Lett.)* **36**, 745–757 (2023).

48. Revie Winston, R. *Uhlig's Corrosion Handbook*, John Wiley and Sons, Inc, (2011).

49. Sun, Y. et al. Understanding the role of alloyed Ni and Cu on improving corrosion resistance of low alloy steel in the simulated Beishan groundwater. *J. Mater. Sci. Technol.* **130**, 124–135 (2022).

50. Samper, J., Lu, C. & Montenegro, L. Reactive transport model of interactions of corrosion products and bentonite. *Phys. Chem. Earth* **33**, 306–316 (2008).

51. Brigatti, M. F., Colonna, S., Malferrari, D., Medici, L. & Poppi, L. Mercury adsorption by montmorillonite and vermiculite: a combined XRD, TG-MS, and EXAFS study. *Appl. Clay Sci.* **28**, 1–8 (2005).

52. Li, Y., Wang, X. & Wang, J. Cation exchange, interlayer spacing, and thermal analysis of Na/Ca-montmorillonite modified with alkaline and alkaline earth metal ions. *J. Therm. Anal. Calorim.* **110**, 1199–1206 (2012).

53. Ferrage, E., Lanson, B., Sakharov, B. A. & Drits, V. A. Investigation of smectite hydration properties by modeling experimental X-ray diffraction patterns. Part I. Montmorillonite hydration properties. *Am. Mineral.* **90**, 1358–1374 (2005).

54. Ferrage, E. et al. Investigation of dioctahedral smectite hydration properties by modeling of X-ray diffraction profiles: influence of layer charge and charge location. *Am. Mineral.* **92**, 1731–1743 (2007).

55. Johnstoni, J. H. & Cardile, C. M. ^{57}Fe Mössbauer spectroscopic study of montmorillonites: a new interpretation. *Clays Clay Miner* **34**, 307–313 (1986).

56. Muller, F., Besson, G., Manceau, A., Drits, V. A. J. P. & Minerals, C. O. Distribution of isomorphous cations within octahedral sheets in montmorillonite from Camp-Bertaux. *Phys. Chem. Miner.* **24**, 159–166 (1997).

57. Chaves, L. H. G., Curry, J. E., Stone, D. A., Carducci, M. D. & Chorover, J. Nickel incorporation in Fe(II, III) hydroxysulfate green rust: effect on crystal lattice spacing and oxidation products. *Rev. Bras. Cienc. Solo* **33**, 1115–1123 (2009).

58. Génin, J.-M. R. Fe(II-II) Hydroxysalt Green Rusts; from corrosion to mineralogy and abiotic to biotic reactions by Mössbauer spectroscopy. *Hyperfine Interact.* **156-157**, 471–485 (2004).

59. Villar, M. V. & Lloret, A. Influence of dry density and water content on the swelling of a compacted bentonite. *Appl. Clay Sci.* **39**, 38–49 (2008).

60. Ye, W. M. et al. Temperature effects on the swelling pressure and saturated hydraulic conductivity of the compacted GMZ01 bentonite. *Environ. Earth Sci.* **68**, 281–288 (2013).

61. Pusch, R. Mineral-water interactions and their influence on the physical behavior of highly compacted Na bentonite. *Can. Geotech. J.* **19**, 381–387 (1982).

62. Ye, W. et al. Features and modelling of time-evolution curves of swelling pressure of bentonite. *Chin. J. Geotech. Eng* **42**, 29–36 (2020).

63. Cosultchi, A., Rossbach, P. & Hernandez-Calderon, I. XPS analysis of petroleum well tubing adherence. *Surf. Interface Anal.* **35**, 239–245 (2003).

64. Chen, L. et al. Investigation of the thermal-hydro-mechanical (THM) behavior of GMZ bentonite in the China-Mock-up test. *Eng. Geol.* **172**, 57–68 (2014).

65. Xiang, G. S., Fang, Y. & Xu Y, F. Swelling characteristics of GMZ01 bentonite affected by cation exchange reaction. *J. Zhejiang Univ. (Eng. Sci.)* **51**, 931–936 (2017).

66. Mystkowskl, K., rodon, J. S. & Elsass, F. Mean thickness and thickness distribution of smectite crystallites. *Clay Miner* **35**, 545–557 (2000).

67. Osacký, M. et al. Mineralogical and physico–chemical properties of bentonites from the Jastrabá Formation (Kremnické vrchy Mts., Western Carpathians). *Geol. Carpathica* **70**, 433–445 (2019).

AUTHOR CONTRIBUTIONS

Y.S.: methodology, investigation, formal analysis, writing - original draft, writing - review & editing. Y.Z.: formal analysis. X.W.: funding acquisition, methodology, formal analysis, writing - review & editing. J.D.: funding acquisition, conceptualization, writing - original draft, writing - review & editing. N.C.: formal analysis. Q.R.: formal analysis. J.W.: formal analysis. W.K.: conceptualiztion.

COMPETING INTERESTS

ADDITIONAL INFORMATION

Correspondence and requests for materials should be addressed to Xin Wei or Junhua Dong.

Reprints and permission information is available at http://www.nature.com/reprints

Publisher's note Springer Nature remains neutral with regard to jurisdictional claims in published maps and institutional affiliations.